Structural and electronic phase transitions of $Co_2Te_3O_8$ spiroffite under high pressure

Nana Li,[1] Bouchaib Manoun,[2,3] Youssef Tamraoui,[3] Qian Zhang,[1] Haini Dong,[1] Yuming Xiao,[4] Paul Chow,[4] Peter Lazor,[5] Xujie Lü,[1] Yonggang Wang,[1] and Wenge Yang[1,*]

[1]*Center for High Pressure Science and Technology Advanced Research, Shanghai 201203, China*

[2]*Université Hassan 1er, Laboratoire des Sciences des Matériaux, des Milieux et de la modélisation (LS3M), FST Settat, Morocco*

[3]*Materials Science and Nano-Engineering, Mohammed VI Polytechnic University, Lot 660 Hay Moulay Rachid, Ben Guerir, Morocco*

[4]*High Pressure Collaborative Access Team (HPCAT), Advanced Photon Source, Argonne National Laboratory, Argonne, Illinois 60439, USA*

[5]*Department of Earth Sciences, Uppsala University, SE-752 36 Uppsala, Sweden*

(Received 26 April 2019; revised manuscript received 30 May 2019; published 12 June 2019)

The structural and electronic phase transitions of $Co_2Te_3O_8$ spiroffite have been studied with a suite of *in situ* high-pressure characterization techniques including synchrotron x-ray diffraction, Raman, x-ray emission spectroscopy, UV-vis absorption, and electrical transport measurement. Two pressure-induced phase transitions were observed at about 6.9 and 14.4 GPa. The first transition is attributed to a small spin transition of Co along with discontinuity in unit-cell volume change, while the second one represents a first-order phase transition with a volume collapse of 4.5%. The latter transition is accompanied by the relaxation of distortion in CoO_6 octahedron, which enhances the crystal-field strength inhibiting the occurrence of spin transition. What is more, the competition between contributions of electrons and oxygen ion to the overall conductivity is observed and affected by the phase transition under high pressure. This demonstration provides insights into the relationship between the lattice-structural and spin degrees of freedom, and highlights the impact of pressure on the control of structural and electronic states of a given material for optimized functionalities.

DOI: 10.1103/PhysRevB.99.245125

I. INTRODUCTION

Spin crossover (SCO) materials offer a fascinating route towards the realization of molecular spintronics due to their bistability in their spin states [1–7], which can be manipulated or switched reversibly with external stimuli like pressure, temperature, light, electric, or magnetic fields [8–12]. Among them, application of external pressure is considered as an effective tool for tuning their crystalline structures, and electronic configurations specifically on the SCO metal site and thus their performances [13–23]. SCO correlates with several degrees of freedom including charge, orbital, lattice, and close proximity of different energy scales among them and then leads to strong modification on magnetic, electronic, optical, and other properties in the corresponding systems [24–28].

The widespread acceptance of ligand field theory in coordination chemistry promotes the fundamental understanding on the structural, spectral, and electronic properties of SCO materials [29,30]. Since the *d-d* optical absorption spectra are very sensitive to the detailed geometry at the metal atom, interest in the ligand field splitting naturally accompanies structural studies of transition-metal compounds [31]. For example, the absorption *d-d* spectra can give evidence of the Co^{2+} ions occupying the D_{2h} anatase cation substitution sites with a $^4E(^4T_{1g})$ low-symmetry ground state in Co^{2+}-doped TiO_2 [32]. Optical absorption spectroscopy at high pressure shows that the Mn^{3+} occurs with the spin transition in $CsMnF_4$ when the high-spin ^5E free energy surpasses the low-spin $^3T_1$ free energy [33]. Therefore, the study on optical properties of SCO materials can provide guides for a better understanding of the electronic or spin state based on the ligand field splitting.

At ambient conditions, $Co_2Te_3O_8$ is a colored spiroffite with transition-metal ions in their unusual oxidation states (Co^{2+} and Te^{4+}) and crystallizes in a monoclinic $C2/c$ symmetry [34,35]. This structure type is based on slabs containing Te_2O_6 groups joined by Co^{2+} cations. These Te_2O_6 groups are made up of two edge-sharing TeO_{3+1} polyhedra. The shift of the lone-pair cation Te^{4+} ($5s^1$) out of the center of its coordination polyhedron results in an asymmetric coordination environment and a structural distortion, which can lead to a variety of interesting physical properties such as nonlinear optical second-harmonic generation, piezoelectricity, and ferroelectricity [36,37]. Pressure as an external stimulus can cause the shift of Te^{4+} ions. Also, the pressure-induced spin reconfiguration of the Co cation has a significant effect on the property of materials [38]. In the case of $Co_2Te_3O_8$, both Co^{2+} and Te^{4+} ions could undergo a pressure-induced spin-state transition or shift, which may also lead to structural instability and an electronic phase transition. Moreover, for Co^{2+} with an octahedral coordination environment in $Co_2Te_3O_8$, there are three distinct band systems which are assumed to originate from the three spin-allowed *d-d* transition of Co^{2+}:$^4T_{1g}\rightarrow{}^4T_{2g}$, $^4T_{1g}\rightarrow{}^4A_{2g}$, and $^4T_{1g}\rightarrow{}^4T_{1g}(^4P)$ [32,34]. The absorption spectra resulting from these spin-allowed *d-d* transitions can give a better understanding of the electronic state of $Co_2Te_3O_8$ spiroffite at high pressure. In this study, we used optical absorption probe (UV-vis absorption

*yangwg@hpstar.ac.cn

 ©2019 American Physical Society

spectroscopy), crystal structural probe [Raman, synchrotron x-ray diffraction (XRD)], electronic spin-state probe [x-ray emission spectroscopy (XES)], and transport measurements [alternating-current (ac) impedance spectroscopy and direct-current (dc) resistance) to explore the interplay between the spin and lattice under pressure effect on the crystal-field splitting in the CoO_6 ligand in $Co_2Te_3O_8$ spiroffite phase. Two structure phase transitions displaying changes of the spin state of Co and the corresponding crystalline structures were observed under high pressure. The competition between contributions of electrons and oxygen ion to the overall conductivity is also observed under high pressure.

II. EXPERIMENTAL DETAILS

A. Sample preparation

Single-phase $Co_2Te_3O_8$ powder was prepared by the standard solid-state reaction method. According to the following chemical reaction:

$$2CoCl_2 \cdot 6H_2O + 3TeO_2 \rightarrow Co_2Te_3O_8 + 10H_2O\uparrow + 4HCl\uparrow,$$

stoichiometric amounts of a high-purity powder of $CoCl_2 \cdot 6H_2O$, and TeO_2 were mixed in an agate mortar, placed in an alumina crucible, and calcined at 500 °C for 24 h, 650 °C for 24 h, and 750 °C for 24 h. The samples were reground in each step to insure the homogeneity. X-ray diffraction (XRD) on the pristine sample confirmed a pure $Co_2Te_3O_8$ spiroffite phase with space group $C2/c$ symmetry and lattice parameters of $a = 12.6998$ Å, $b = 5.2145$ Å, $c = 11.6350$ Å, and $\beta = 99.02°$, consistent with the literature report [34].

B. *In situ* high-pressure characterizations

A suite of *in situ* high-pressure characterization tools were utilized to probe the crystalline and electronic structure, and physical properties. For studying the structural evolution under pressure, *in situ* high-pressure XRD in angle-dispersive geometry was performed at the beamline 16BM-D of the Advanced Photon Source (APS), Argonne National Laboratory (ANL) with a wavelength $\lambda = 0.4246$ Å. Symmetric diamond-anvil cells (DAC) with an anvil culet size of 300 μm and rhenium gaskets were used. Neon was used as the pressure medium and pressure was determined by the ruby luminescence method [39]. Rietveld refinements of crystal structures at various pressures were performed using the General Structure Analysis System (GSAS) and graphical user interface EXPGUI package [40]. The high-pressure Raman spectra were measured by a Raman spectrometer using a 532-nm excitation laser with 3 mW of power. The preparation of sample and DAC for the Raman study was the same as for the XRD measurement.

To monitor the spin state and the crystal-field splitting energy Δ_o at various high pressures, XES of Co-K_β and the high-pressure UV-vis absorption measurements were conducted at 16ID-D beamline of APS, ANL, and Center for High Pressure Science & Technology Advanced Research with Ocean Optics QE65000 scientific-grade spectrometer, respectively. In XES experiments, helium pipes were used at both incident and emission x-ray paths to minimize the air scattering and absorption. Symmetric diamond-anvil cells with 300-μm culet-sized anvils were used with neon pressure medium. Beryllium gaskets were preindented to 40 μm thick and drilled with a 150-μm diameter hole as sample chambers. The pressure was calibrated by the ruby luminescence method [39]. For the UV-vis absorption measurements, the precompressed rhenium gasket, loading sample, and pressure calibration are the same as the high-pressure XRD experiments. Silicone oil was used as the pressure-transmitting medium.

For the related transport characterization, we performed ac impedance spectroscopy and dc resistance under high pressure. ac impedance spectroscopy in the frequency range of 0.01 Hz–10 MHz under high pressure was conducted using Zahner impedance analyzers. dc resistance was conducted using a Keithley 6517 electrometer. Two-probe ac impedance spectroscopy and dc resistance measurements were performed by arranging two Pt electrodes on the diamond culet in the DAC loaded with the $Co_2Te_3O_8$ sample. Pressure medium was not used in these two experiments.

III. RESULTS AND DISCUSSION

A. Structure evolution

The ambient crystal structure of spiroffite $Co_2Te_3O_8$ with $C2/c$ space group consists of divalent Co^{2+} and tetravalent Te^{4+} [34,35]. The edge-shared octahedral Co_2O_{10} dimmers are interlinked through corners, and Te^{4+} ions occupy the irregular fourfold coordination sites, as shown in Fig. 1(a). In situ high-pressure XRD measurements on $Co_2Te_3O_8$ were carried out up to 35.1 GPa and selected patterns are displayed in Fig. 1(b). At 6.9 GPa, the relative intensity between the lattice planes (20−2) and (11−1) showed a sharp change. Besides, a peak around 7.5° as shaded with gray color emerged, while the low-pressure lattice planes (−311) and (−204) disappeared around 14.4 GPa. These features indicate a possible phase transition in $Co_2Te_3O_8$ under high pressure. We carried out the Rietveld refinements for all the XRD patterns. Although the crystalline symmetry remains the same, the obtained unit-cell volumes and lattice parameters at different pressures present discontinuities at 6.9 and 14.4 GPa as shown in Figs. 1(c) and Fig. 1(d). Two typical refinement results at 0.8 and 20.0 GPa are shown in Supplemental Material (Fig. S1 [41]). We fitted the experimental *P-V* points by a third-order Birch-Murnaghan equation of state (EOS) [42]. Below 6.9 GPa, we obtained zero-pressure volume $V_0 = 767.94$ Å^3, bulk modulus $B_0 = 40(2)$ GPa, and its pressure derivative $B_0' = 6.4$. From the *P-V* curve in Fig. 1(c), it is obvious that the compressibility becomes lower above 6.9 GPa, indicating a possible electronic phase transition. The EOS fitting between 6.9 and 14.4 GPa yields $B_0 = 88(5)$ GPa and $B_0' = 7.0$, with $V_0 = 719.57$ Å^3. We also obtained the coefficient of compressibility β by $\beta = -\frac{1}{V}(\frac{\partial V}{\partial P})_T$ at 6.9 GPa and the values are 0.011 for low-pressure phase and 0.007 for high-pressure phase. The crystal structure of spiroffite $Co_2Te_3O_8$ remains the same space group up to 35.1 GPa, but with a substantial volume collapse around 4.5% at 14.4 GPa, a typical first-order isostructural transition. For the high-pressure monoclinic phase, the bulk modulus B_0 is 89(12) GPa and its pressure derivative $B_0' = 4.2$ with $V_0 = 687.32$ Å^3.

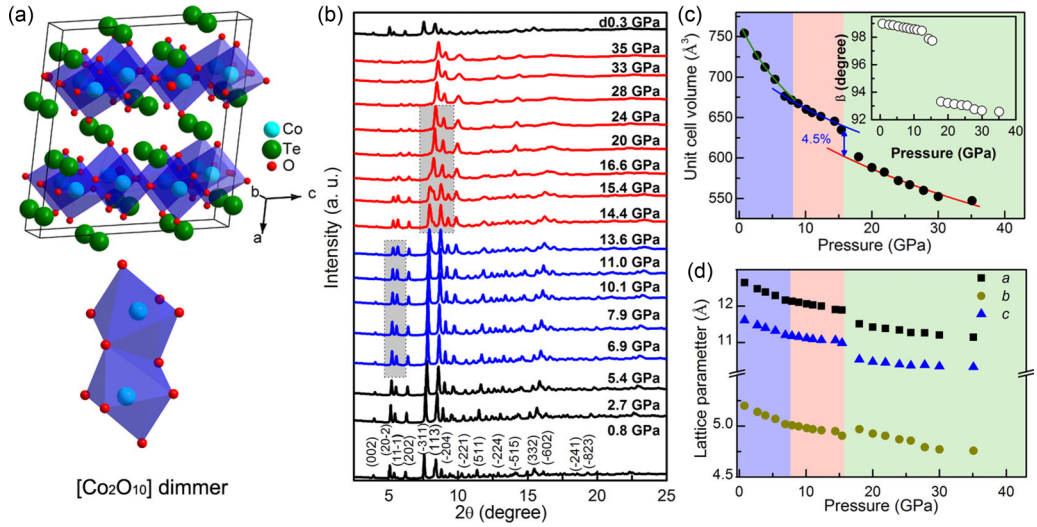

FIG. 1. Structural evolution of $Co_2Te_3O_8$ under high pressure probed by synchrotron x-ray diffraction. (a) Atomic arrangement of $Co_2Te_3O_8$ with *C2/c* space group. (b) X-ray diffraction spectra at room temperature and high pressure; incident x-ray wavelength $\lambda = 0.4246$ Å. (c), (d) Unit-cell volume and lattice parameters as a function of pressure. In (b), the gray shadow areas indicate changes in the XRD curves. In (c), the inset picture shows the angle β as a function of pressure. In (c), the lines represent fitting results of the third-order Birch-Murnaghan equation of state for three pressure regions.

This structural phase transition is reversible upon pressure release.

Results from high-pressure Raman measurements were consistent with the aforementioned discovery from the XRD measurements, as shown in Fig. 2. Major peaks are assigned as follows [43]: 640 cm^{-1} (υ_{11}) and 715 cm^{-1} (υ_{13}) are attributed to the Te-O antisymmetric stretching and $(Te_2O_5)^{2-}$ symmetric stretching vibration, respectively; two Raman bands at 320 cm^{-1} (υ_8) and 360 cm^{-1} (υ_9) are attributed to the Te-O bending vibrations. Two shoulder peaks are also noted at 743 cm^{-1} (υ_{14}) and 756 cm^{-1} (υ_{15}). As shown in Fig. 2(a), a small peak at 520 cm^{-1} (υ_{16}) appeared at around 7 GPa, indicating a minute change of the crystal structure. Besides, four peaks at 106 cm^{-1} (υ_{17}), 220 cm^{-1} (υ_{18}), 249 cm^{-1} (υ_{19}), and 500 cm^{-1} (υ_{20}) appeared along with the disappearance of other Raman modes around 15.6 GPa as shown in Fig. 2(a). These observations concur with two phase transitions at around 7 and 15 GPa from the XRD results. Figure 2(b) summarizes the Raman shift changes with pressure. After 27 GPa as shown in Figs. 2(a) and 2(b), the intensity of all Raman bands decrease and some of the Raman bands disappeared caused by the nonhydrostatic stresses and other factors involving grain-size reduction and the increased local stain effect [44,45].

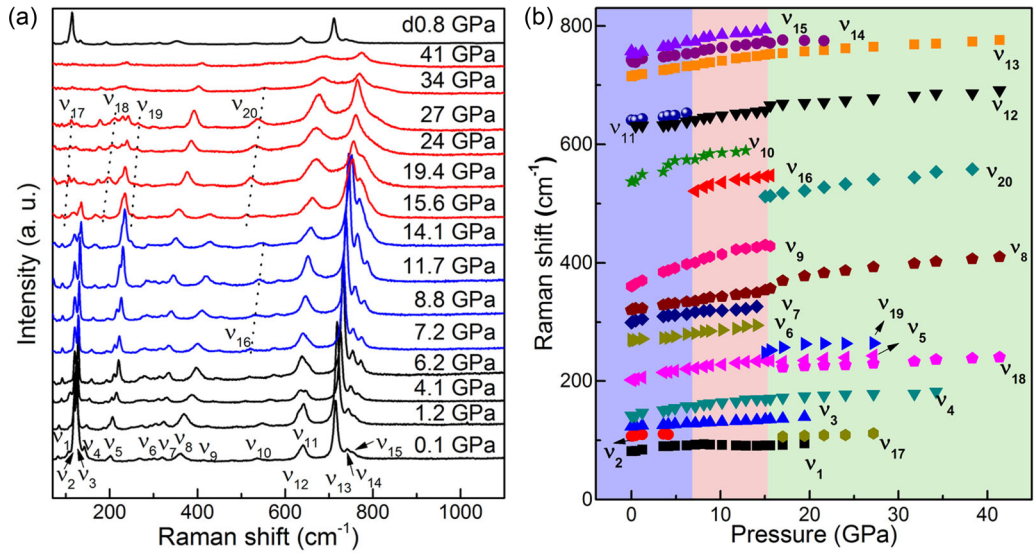

FIG. 2. Changes of Raman bands in $Co_2Te_3O_8$ under high pressure. (a) Selected Raman spectra under high pressure. The dotted lines indicate peaks in the spectra. (b) Raman mode frequencies at different pressures.

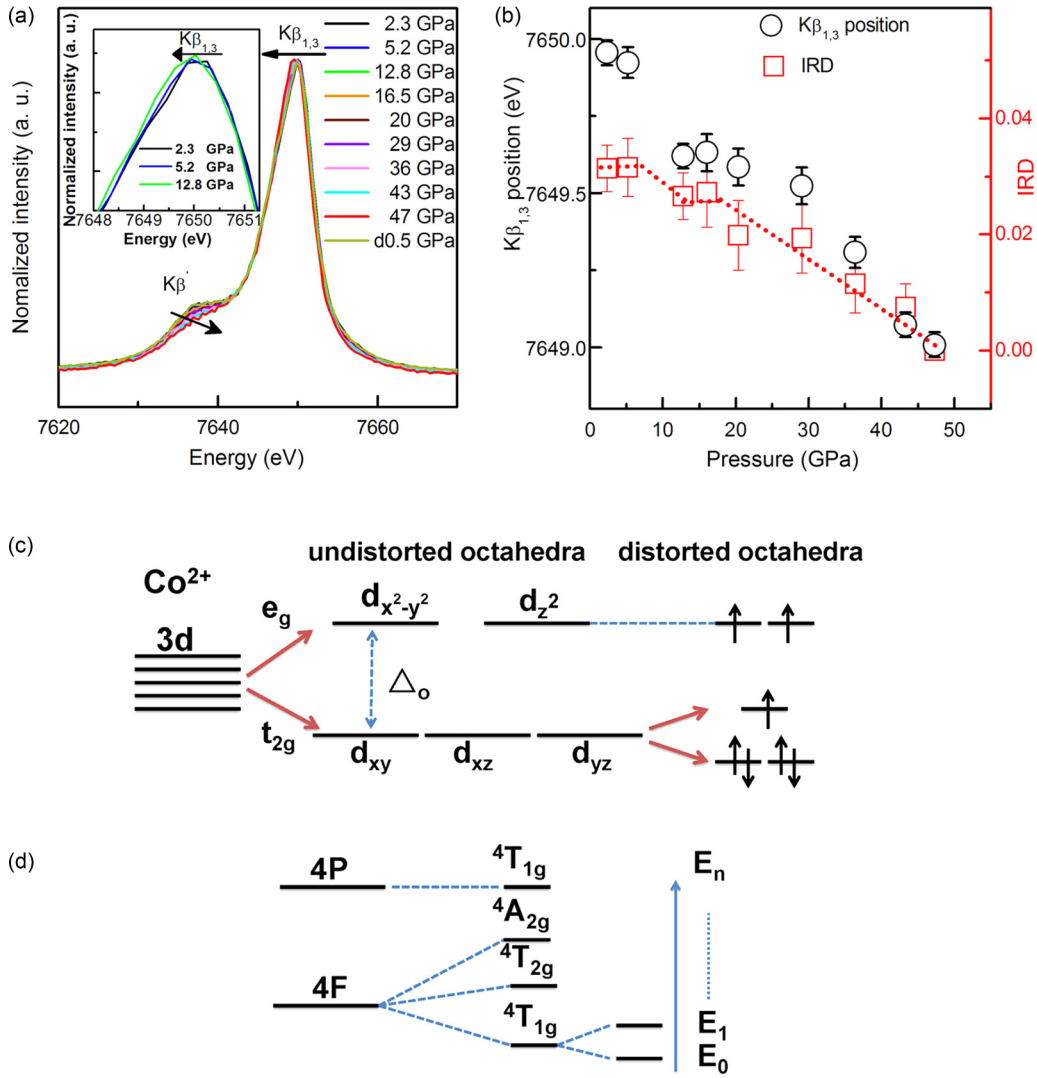

FIG. 3. Spin states of Co under high pressure. (a) XES spectrum of Co at different pressures. The inset in (a) magnified is the enlargement of the K$\beta_{1,3}$ peaks at 2.3, 5.2, and 12.8 GPa. (b) $K_{\beta 1,3}$ position and IRD values of Co under high pressure. (c) Schematic d-orbital splitting diagram for Co^{2+} in the CoO_6 octahedra. (d) Term diagram shows the splitting of the Co^{2+} free-ion terms in the CoO_6 octahedral ligand fields.

B. Spin transition of Co under high pressure

The structural transition in $Co_2Te_3O_8$ will induce distortions in the CoO_6 octahedra, and thus affect the crystal-field splitting of the Co^{2+} $3d^7$ orbital in CoO_6 ligand field under high pressure. A pressure-induced increase in the crystal-field splitting can largely affect the spin configuration to minimize the total energy [46]. XES has been utilized as a powerful tool to probe the spin states of transition metals. We conducted XES measurements on the Co K_β emission of $Co_2Te_3O_8$ under high pressure. The pressure-dependent $K_{\beta 1,3}$ and $K_{\beta'}$ emission spectra of Co are shown in Fig. 3(a). All spectra are normalized to the integrated area. The K_β emission originates from the transition of 1s core hole from a 3p level [47,48]. Due to the net magnetic moment (μ) effect on the 3d valence shell [49,50], the K_β emission spectrum is split into the main line $K_{\beta 1,3}$ and a satellite line $K_{\beta'}$. The satellite intensity of $K_{\beta'}$ is proportional to the net spin of the 3d shell of the transition metal [51,52].

The starting materials have Co^{2+} ($S = 3/2$) at its high-spin (HS) state. As shown in Fig. 3(a), the $K_{\beta 1,3}$ peak shifts to the lower energy and the intensity of the $K_{\beta'}$ decreases upon pressure increase. We applied the integrated relative difference (IRD) method to analyze the XES spectra [53]. Figure 3(b) shows the IRD values for Co at different pressures. The decrease in IRD with pressure in the range 5 to 12 GPa indicates a significant loss of magnetic moment in $Co_2Te_3O_8$. Above 12 GPa, the spin values remain constant until pressure reaching 16 GPa, when their sharp decrease implies a spin transition in Co. Even so, a net spin of the 3d shell for Co persists, as evidenced by small $K_{\beta'}$-peaks shoulders in the XES spectra at the highest pressures.

At ambient pressure, Co^{2+} in $Co_2Te_3O_8$ has a $3d^7$ configuration; seven 3d electrons occupy the d_{xy}, d_{xz}, d_{yz}, $d_{x^2-y^2}$, and $d_z{}^2$ orbitals in a HS configuration ($t_{2g}^5\, e_g^2$) based on Hund's rule. Five electrons in the t_{2g} orbitals exhibit an asymmetric configuration distorting the CoO_6 octahedra and then t_{2g} splits into double-degenerate and nondegenerate orbitals as shown in Fig. 3(c). The net spin magnetic moment is mainly controlled by the competition between the crystal-field splitting Δ_o [favoring the low spin (LS) state] and the intra-atomic

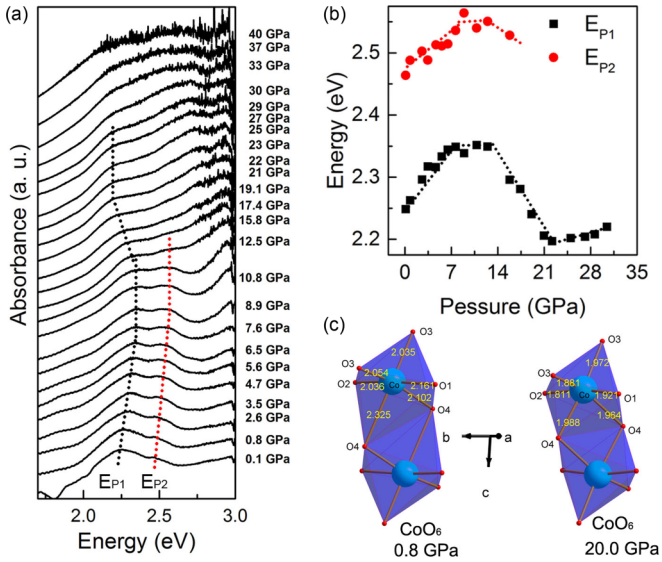

FIG. 4. Crystal-splitting energy changes under high pressure. (a) Absorption spectra of $Co_2Te_3O_8$ under high pressure. The guiding lines indicate the evolution of the E_{P1} and E_{P2} peak positions. (b) Pressure dependence of the absorption peaks E_{P1} and E_{P2}. (c) Comparison of CoO_6 octahedron distortions at 0.8 and 20.0 GPa.

exchange term J (favoring the HS state), but only Δ_o is sensitive to external pressure. In an octahedral coordination environment the optical spectrum of Co^{2+} is expected to consist of three spin-allowed optical absorption bands arising from the ${}^4T_{1g}\rightarrow{}^4T_{2g}$, ${}^4T_{1g}\rightarrow{}^4A_{2g}$, and ${}^4T_{1g}\rightarrow{}^4T_{1g}({}^4P)$ transitions as shown in Fig. 3(d). Δ_o can be obtained by the splitting energy of ${}^4T_{1g}(F)\rightarrow{}^4T_{1g}(P)$ ligand field. Therefore, to understand the spin changes under high pressure, we performed high-pressure UV-vis absorption measurements on $Co_2Te_3O_8$.

An undistorted CoO_6 octahedron typically shows a broad absorption in the visible range, spreading over 2 to 3 eV with a maximum value around 2.5 eV, which corresponds to ${}^4T_{1g}(F)\rightarrow{}^4T_{1g}(P)$ and ${}^4T_{1g}(F)\rightarrow{}^4A_{2g}$ transitions [32,34]. In $Co_2Te_3O_8$, it has one main absorption peak at around 2.3 eV (E_{P1}) with a shoulder at 2.4 eV (E_{P2}), which indicates a distortion of the CoO_6 octahedron, as shown in Fig. 4(a) [31,34]. Upon pressure increase, absorption energies E_{P1} and E_{P2} shift to higher values as shown in Fig. 4(b). This indicates that the crystal-field splitting energy Δ_o increases upon compression. Around 7.6 GPa, the larger Δ_o makes Co undergo the first spin transition, as corroborated by the sharp decrease of IRD values between 5.2 and 12.8 GPa. This electronic phase transition was also observed in the XRD experiments around 6.9 GPa through discontinuous changes in both unit-cell volume and lattice parameters as shown in Figs. 1(c) and 1(d). From 7.6 to 14 GPa, absorption energies E_{P1} and E_{P2} remain nearly constant. Thus the spin values do not change as the IRD value of Co still remains constant in this pressure range. From 15.8 and 23 GPa, the absorption energy E_{P1} shows a sharp decrease, while the band corresponding to absorption energy E_{P2} disappears. This indicates a big change occurs in the ligand field of Co in $Co_2Te_3O_8$. According to the XRD results, a first-order structural transition with a sharp volume collapse of 4.5% occurs at around 14.4 GPa. In order to get further insight into the ligancy changes of Co in $Co_2Te_3O_8$, detailed structural parameters at 0.8 and 20.0 GPa are provided in the Supplemental Material (Table S1 [41]). The refined bond lengths of CoO_6 octahedron at these two pressures are shown in Fig. 4(c). Zhao *et al.* introduced a standard infinitesimal strain tensor to describe the distortion of the octahedron in $NaMgF_3$ perovskites [54]. Here, we introduce a scale factor

$$\delta = \sqrt{\frac{1}{6}\sum_{i=1,6}\left(\frac{d^i_{\mathrm{Co-O}} - \langle d_{\mathrm{Co-O}}\rangle}{d^i_{\mathrm{Co-O}}}\right)^2}$$

to describe the distortion from the regular octahedron ($\delta = 0$) with all bonding distance between Co and O in CoO_6 octahedron. The larger δ is, the more severe distortion occurs. In $Co_2Te_3O_8$, δ actually decreases from 0.046 at 0.8 GPa to 0.033 at 20.0 GPa, which relaxes the CoO_6 octahedron distortion and induces large changes in the ligancy of Co. This, in turn, influences the d-orbital splitting and causes a major decrease in the crystal-field splitting Δ_o. When $Co_2Te_3O_8$ has been completely transformed into the high-pressure monoclinic phase above 25 GPa, the crystal-field splitting Δ_o in the ligand field begins to increase again at still higher compressions, possibly inducing a spin transition of Co at some point.

C. Electrical property at high pressure

ac impedance spectroscopy and dc resistance measurements were conducted up to 49 GPa to investigate the electrical property of $Co_2Te_3O_8$ under high pressure. The impedance data are modeled by one equivalent series circuit consisting of a resistor (R) and constant phase element [55]. By fitting the data using the ZVIEW impedance analysis software [56], we obtain the grain contribution to the ac resistance, as shown in Fig. 5. With increasing pressure, the grain ac resistance increases. The electronic property measured by the impedance method originates mainly from the oxygen ion conduction. Upon compression, the decreased interatomic distance reduced the oxygen ion conductivity, thus increasing the resistance. From 10 to 20 GPa, where the structural phase transition takes place, the grain resistance remains almost constant. This wide pressure range (about 10 GPa) where

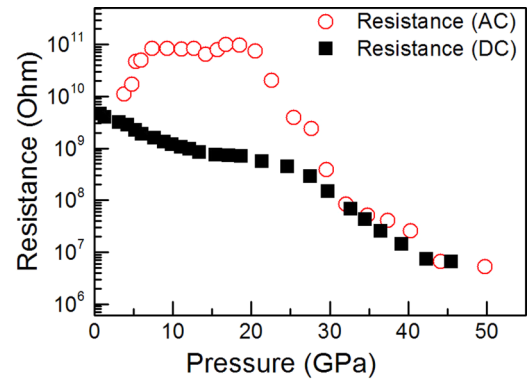

FIG. 5. Electric transport property of $Co_2Te_3O_8$ under high pressure. Resistance measured from ac impedance spectroscopy and dc measurements.

the phase transition occurred in this experiment is caused by the nonhydrostatic effects. Above 20 GPa, after the transition to the high-pressure monoclinic phase is completed, the resistance values based on the ac impedance measurements show a sharp drop. Due to the changes of the Co ligancy, the ionic conduction is taken over by the electronic conduction. This picture agrees well with the results of the dc resistance measurements, as shown in Fig. 5. With pressure increase, the electronic resistance decreases and shows a small discontinuous change at around 20 GPa caused by the structural phase transition. The typical Nyquist plots for the polycrystalline $Co_2Te_3O_8$ under high pressure are shown in the Supplemental Material (Fig. S2 [41]).

IV. CONCLUSIONS

In conclusion, by using multiple *in situ* high-pressure techniques, we investigated the structural and electronic properties of $Co_2Te_3O_8$. Two pressure-induced phase transitions were observed. First, $Co_2Te_3O_8$ displays an electronic phase transition caused by the spin transition of Co at around 6.9 GPa. Upon further compression, $Co_2Te_3O_8$ goes through another first-order phase transition with a volume collapse of 4.5%, accompanied by a major change in the ligand field of Co at about 14 GPa. It results in a sharp decrease in the crystal-field energy. So, the IRD values are almost constant from 12 to 16 GPa. When $Co_2Te_3O_8$ transforms into the high-pressure monoclinic phase completely, the crystal-field splitting energy Δ_o in the ligand field begins to increase again above 25 GPa and a spin transition of Co to the low-spin state takes place. Furthermore, the electronic conduction replaces the oxygen ion conduction as a leading conduction mechanism following the first-order structural phase transition around 20 GPa. Our study demonstrates the great versatility of spiroffites and their potential to unravel the exciting interplay of different degrees of freedom in SCO compounds.

ACKNOWLEDGMENTS

This work was financially supported by the National Nature Science Foundation of China (Grants No. 51527801 and No. U1530402). HPCAT operations are supported by DOE-NNSA under Award No. DE-NA0001974 and DOE-BES under Award No. DE-FG02-99ER45775, with partial instrumentation funding by NSF. The gas loading was performed at GeoSoilEnviroCARS, APS, ANL, supported by Grants No. EAR-1128799 and No. DE-FG02-94ER14466 and EAR-1128799. APS is supported by DOE-BES, under Contract No. DE-AC02-06CH11357.

[1] P. E. Figgins and D. H. Busch, J. Am. Chem. Soc. **82**, 820 (1960).
[2] M. A. Robinson, J. D. Curry, and D. H. Busch, Inorg. Chem **2**, 1178 (1963).
[3] R. C. Stoufer, D. H. Busch, and W. B. Hadley, J. Am. Chem. Soc. **83**, 3732 (1961).
[4] K. Madeja and E. König, J. Inorg. Nucl. Chem. **25**, 377 (1963).
[5] A. Fert, Rev. Mod. Phys. **80**, 1517 (2008).
[6] K. Moth-Poulsen and T. Bjornholm, Nat. Nanotechnol. **4**, 551 (2009).
[7] H. Song, M. A. Reed, and T. Lee, Adv. Mater. **23**, 1583 (2011).
[8] L. Cambi and L. Szegö, Ber. Dtsch. Chem. Ges. B **64**, 2591 (1931).
[9] S. Decurtins, P. Gütlich, C. Köhler, H. Spiering, and A. Hauser, Chem. Phys. Lett. **105**, 1 (1984).
[10] M. A. Halcrow, *Spin-Crossover Materials: Properties and Applications* (Wiley & Sons, New York, 2013).
[11] T. G. Gopakumar, F. Matino, H. Naggert, A. Bannwarth, F. Tuczek, and R. Berndt, Angew. Chem. Int. Ed. **51**, 6262 (2012).
[12] D. Collison, C. D. Gaener, C. M. Mcgrath, J. F. W. Mosselmans, M. D. Roper, J. M. W. Seddon, E. Sinn, and N. A. Young, J. Chem. Soc., Dalton Trans. **22**, 4371 (1997).
[13] A. B. Gaspar, G. Molnárb, A. Rotaruc, and H. J. Shepherdd, C. R. Chim. **21**, 1095 (2018).
[14] H. G. Drickamer, Int. Rev. Phys. Chem. **2**, 171 (1982).
[15] E. Konig, Struct. Bonding **76**, 51 (1991).
[16] G. J. Long, L. W. Becker, W. Laurie, and B. B. Hutchinson, Adv. Chem. Ser. **194**, 453 (1981).
[17] C. P. Kohler, R. Jakobi, E. Meissner, L. Wiehl, H. Spiering, and P. Gütlich, J. Phys. Chem. Solids **51**, 239 (1990).
[18] G. J. Long and B. B. Hutchinson, Inorg. Chem. **26**, 608 (1987).
[19] J. Pebler, Inorg. Chem. **22**, 4125 (1983).
[20] J. C. Crowhurst, J. M. Brown, A. F. Goncharov, and S. D. Jacobsen, Science **319**, 451 (2008).
[21] J.-Y. Yang, C. Terakura, M. Medarde, J. S. White, D. Sheptyakov, X.-Z. Yan, N.-N. Li, W.-G. Yang, H.-L. Xia, J.-H. Dai, Y.-Y. Yin, Y.-Y. Jiao, J.-G. Cheng, Y.-L. Bu, Q.-F. Zhang, X.-D. Li, C.-Q. Jin, Y. Taguchi, Y. Tokura, and Y.-W. Long, Phys. Rev. B **92**, 195147 (2015).
[22] A. F. Goncharov, V. V. Struzhkin, and S. D. Jacobsen, Science **312**, 1205 (2006).
[23] S. A. S. Kimber, A. Kreyssig, Y. Z. Zhang, H. O. Jeschke, R. Valentí, F. Yokaichiya, E. Colombier, J. Yan, T. C. Hasen, T. Chatterji, R. J. McQueeney, P. C. Canfield, A. I. Goldman, and D. N. Argyriou, Nat. Mater. **8**, 471 (2009).
[24] O. Kahn and C. M. Jay, Science **279**, 44 (1998).
[25] F. Wasser, A. Schneidewind, Y. Sidis, S. Wurmehl, S. Aswartham, B. Buchner, and M. Braden, Phys. Rev. B. **91**, 060505(R) (2015).
[26] M. Mikolasek, M. D. Manrique-Juarez, H. J. Shepherd, K. Ridier, S. Rat, V. Shalabaeva, A. C. Bas, I. E. Collings, F. Mathieu, J. Cacheux, T. Leichle, L. Nicu, W. Nicolazzi, L. Salmon, G. Molnar, and T. Leichlé, J. Am. Chem. Soc. **140**, 8970 (2018).
[27] C. Lochenie, K. Schotz, F. Panzer, H. Kurz, B. Maier, F. Puchtler, S. Agarwal, A. Kohler, and B. Weber, J. Am. Chem. Soc. **140**, 700 (2018).
[28] D. A. Reed, D. J. Xiao, M. I. Gonzalez, L. E. Darago, Z. R. Herm, F. Grandjean, and J. R. Lomh, J. Am. Chem. Soc. **138**, 5594 (2016).
[29] P. Gutlich and H. A. Goodwin (Eds.), *Spin Corssover Transition Metal Compounds I*, Topics in Current

Chemistry Vol. 223 (Springer, Berlin, Heidelberg, 2004), pp. 1–47.

[30] J. Antonio Barreda-Argüeso, F. Aguado, J. González, R. Valiente, L. Nataf, M. N. Sanz-Ortiz, and F. Rodríguez, J. Phys. Chem. C **120**, 18788 (2016).

[31] A. B. P. Lever, *Inorganic Electronic Spectroscopy* (Elsvier, Amsterdam, 1968).

[32] F. Aguado, F. Rodriguez, and P. Nunez, Phys. Rev. B **76**, 094417 (2007).

[33] J. D. Bryan, S. M. Heald, S. A. Chambers, and D. R. Gamelin, J. Am. Chem. Soc. **126**, 11640 (2004).

[34] S. Tamilarasan, D. Sarma, S. Bhattacharjee, U. V. Waghmare, S. Natarajan, and J. Gopalakrishnan, Inorg. Chem. **52**, 5757 (2013).

[35] C. R. Feger, G. L. Schimek, and J. W. Kolis, J. Solid State Chem. **143**, 246 (1999).

[36] Y. Porter, K. M. Ok, N. S. P. Bhuvanesh, and P. S. Halasyamani, Chem. Mater. **13**, 1910 (2001).

[37] E. O. Chi, K. M. Ok, Y. Porter, and P. S. Halasyamani, Chem. Mater. **18**, 2070 (2006).

[38] K. Oka, M. Azuma, W. Chen, H. Yusa, A. A. Belik, E. Takayama-Muromachi, M. Mizumaki, N. Ishimatsu, N. Hiraoka, M. Tsujimoto, M. G. Tucker, J. P. Attfield, and Y. Shimakawa, J. Am. Chem. Soc. **132**, 9438 (2010).

[39] H. K. Mao and P. M. Bell, Year Book-Carnegie Inst. Washington **77**, 904 (1978).

[40] A. C. Larson and R. B. Von Dreele, General Structure Analysis System (GSAS), Los Alamos National Laboratory Report No. LAUR 86-748, Los Alamos, NM, 2004.

[41] See Supplemental Material at http://link.aps.org/supplemental/10.1103/PhysRevB.99.245125 for the analysis of XRD and impedance spectroscopy at high pressure.

[42] H. K. Mao, T. Takahashi, W. A. Bassett, G. L. Kinsland, and L. Merrill, J. Geophys. Res. **79**, 1165 (1974).

[43] R. L. Frost, M. J. Dickfos, and E. C. Keeffe, Spectrochim. Acta, Part A **71**, 1663 (1994).

[44] V. S. Bhadram, L. Krishna, E. S. Toberer, R. Hrubiak, E. Greenberg, V. B. Prakapenka, and T. A. Strobel, Appl. Phys. Lett. **110**, 182106 (2017).

[45] X. Lü, W. Yang, Q. Jia, and H. Xu, Chem. Sci. **8**, 6764 (2017).

[46] G. K. Rozenberg, M. P. Pasternak, W. M. Xu, L. S. Dubrovinsky, S. Carlson, and R. D. Taylor, Europhys. Lett. **71**, 228 (2005).

[47] K. Hämäläinen, C. C. Kao, J. B. Hastings, D. P. Siddons, L. E. Berman, V. Stojanoff, and S. P. Cramer, Phys. Rev. B **46**, 14274 (1992).

[48] G. Peng, X. Wang, C. R. Randall, J. A. Moore, and S. P. Cramer, Appl. Phys. Lett. **65**, 2527 (1994).

[49] K. Tsutsumi, H. Nakamori, and K. Ichikawa, Phys. Rev. B **13**, 929 (1976).

[50] G. Peng, F. M. F. Degroot, K. Haemaelaeinen, J. A. Moore, X. Wang, M. M. Grush, J. B. Hastings, D. P. Siddons, and W. H. Armstrong, J. Am. Chem. Soc. **116**, 2914 (1994).

[51] J. M. Chen, S. C. Haw, J. M. Lee, S. A. Chen, K. T. Lu, S. W. Chen, M. J. Deng, Y.-F. Liao, J. M. Lin, B. H. Chen, F. C. Chou, N. Hiraoka, H. Ishii, K. D. Tsuei, and E. Huang, Phys. Rev. B **86**, 045103 (2012).

[52] J. P. Rueff, C. C. Kao, V. V. Struzhkin, J. Badro, J. Shu, R. J. Hemley, and H. K. Mao, Phys. Rev. Lett. **82**, 3284 (1999).

[53] C. S. Yoo, B. Maddox, J. H. P. Klepeis, V. Iota, W. Evans, A. McMahan, M. Y. Hu, P. Chow, M. Somayazulu, D. H¨ausermann, R. T. Scalettar, and W. E. Pickett, Phys. Rev. Lett. **94**, 115502 (2005).

[54] Y. S. Zhao, D. J. Weidner, J. B. Parise, and D. E. Cox, Phys. Earth Planet. Inter. **76**, 1 (1993).

[55] D. C. Sinclair and A. R. West, J. Appl. Phys. **66**, 3850 (1989).

[56] D. Johnson, ZVIEW: *A Software Program for IES Analysis, Version 2.8*, Scribner Associates, Southern Pines, NC, Vol. 200 (2008).